Journal of Molecular Medicine (2026) 104:60
https://doi.org/10.1007/s00109-026-02669-7

JMolMed

ORIGINAL ARTICLE

Integrative multimodal transcriptomics identifies a cancer-associated fibroblast membrane signature for predicting prognosis and therapeutic response in pancreatic ductal adenocarcinoma

Leshi Zhuang[1] · Wei Zhang[2] · Jun Wu[2,3] · Jian Cao[4] · Liang Feng[4] · Shubo Cao[1]

Received: 30 October 2025 / Revised: 25 March 2026 / Accepted: 26 March 2026

Abstract

Cancer-associated fibroblasts (CAFs) are central to the pancreatic ductal adenocarcinoma (PDAC) microenvironment, promoting tumor progression and therapeutic resistance. However, the expression landscape of CAF membrane proteins in PDAC remains poorly defined. We integrated scRNA-seq ($n=33$; 87,949 cells), spatial transcriptomics ($n=2$; 7,011 spots), and bulk RNA-seq ($n=7$; 642 samples) to systematically identify PDAC-specific CAF membrane genes. A LASSO-based Cox model was developed to construct a prognostic signature, PaFMS, and evaluated through multi-cohort validation. Functional enrichment, immune infiltration, drug sensitivity, and immunotherapy response analyses were further conducted. Validation was performed using multiple database-driven analyses. We identified a PDAC-enriched myoCAF-c1 cluster closely associated with epithelial–mesenchymal transition (EMT) and angiogenesis. From this cluster, 33 candidate CAF membrane genes were defined, whose protein–protein interactions were predominantly linked to extracellular matrix organization and collagen remodeling, and spatially colocalized with myoCAF-c1 and EMT regions. An 11-gene prognostic signature, PaFMS that robustly stratified patients across six independent cohorts, achieving high predictive accuracy for overall survival. High-risk patients exhibited proliferative signaling activation, immune suppression, and reduced T/B-cell infiltration. PaFMS was associated with responses to 33 anticancer agents and predicted enhanced benefit from anti–PD-L1 immunotherapy in the low-risk group. Multi-cohort validation confirmed the expression specificity of PaFMS genes, including PLAU, TMEM158, and TRIM59. Together, these findings reveal that myoCAF-c1 promotes angiogenesis and tumor progression, and establish PaFMS as a robust CAF membrane–based prognostic model in PDAC with potential utility for precision prognosis and therapeutic decision-making.

Key messages

- Integrated single-cell, spatial, and bulk RNA-seq analyses identified PDAC-specific CAF membrane genes.
- Discovered a PDAC-enriched myoCAF-c1 subtype linked to EMT and angiogenesis.
- Developed an 11-gene CAF membrane–based prognostic model (PaFMS) validated across six cohorts.
- PaFMS predicts patient survival, drug sensitivity, and immunotherapy response in PDAC.

Keywords Pancreatic cancer · Cancer-associated fibroblast · Prognostic model · Membrane

Introduction

Pancreatic ductal adenocarcinoma (PDAC) remains one of the most lethal malignancies worldwide [1], with a 5-year survival of less than 10% [2]. The absence of reliable biomarkers for early detection [3], combined with the anatomical inaccessibility of the pancreas, poses significant challenges for effective screening [1]. Many PDAC cases are diagnosed at advanced, unresectable stages [4]. Recurrent and metastatic PDAC further worsens clinical outcomes, with liver metastases representing a particularly aggressive and prognostically unfavorable subset [5, 6]. Therefore, delineating the tumor compositional differences between primary PDAC and its liver metastases is critical for guiding novel therapeutic strategies.

Leshi Zhuang, Wei Zhang and Jun Wu contributed equally to this work.

Extended author information available on the last page of the article

Published online: 06 April 2026

The tumor microenvironment (TME) plays a pivotal role in the PDAC progression, with its hallmark desmoplastic stroma forming physical and immunological barriers that foster hypoxia and tumor invasion [7, 8]. The stromal compartment consists of cancer-associated fibroblasts (CAFs) [9, 10], tumor associated endothelial cells (TAEs) [11], which collectively shape a tumor-promoting niche. Among these, CAFs are key contributors by remodeling the extracellular matrix (ECM) [9] and establishing immunosuppressive barriers [12], thereby enhancing therapeutic resistance [13]. Moreover, endothelial cells, such as COL4A1 + TAEs, interact with CAFs and macrophages to facilitate PDAC progression [14]. The CAFs have thus emerged as critical biomarkers and therapeutic targets across multiple malignancies, including breast [12], ovarian [15], lung [16], skin [17], and gastric [18] cancers.

Membrane proteins expressed on the surface of cancer cells and the TME can serve as ideal targets for therapeutic intervention [19, 20]. For example, membrane proteins identified in this context can serve as candidate targets for multiple downstream applications, such as active targeting in drug delivery systems [21], cell-surface–proteomics–guided target discovery [22], the development of targeted therapeutics including antibody–drug conjugates [23], and immune-cell–based strategies such as chimeric antigen receptor (CAR) therapies (including CAR-T and CAR-NK) [20, 24], thereby enabling selective recognition of tumor cells and improved therapeutic precision. A recent study has reported that membrane genes can serve as prognostic markers in lung adenocarcinoma and may potentially guide therapeutic strategies [25]. Moreover, fibroblasts within the TME are increasingly recognized as potential therapeutic targets [26]; for example, anti-fibroblast activation protein (FAP) CAR-T cells have been shown to enhance PDAC tumor clearance in murine models [19, 27]. However, the membrane proteins expressed by CAFs in the PDAC TME remain poorly characterized.

The advent of single-cell sequencing technologies, such as single-cell RNA sequencing (scRNA-seq), has enabled researchers to investigate PDAC at single-cell resolution across various cancer contexts [28–30]. More recently, the emergence of spatial transcriptomics has made it possible to interrogate the PDAC TME within its native spatial context [31–33]. In this study, we integrated publicly available scRNA-seq datasets encompassing PDAC primary tumors, adjacent normal pancreatic tissues, and PDAC liver metastases [30, 34, 35], together with spatial transcriptomic data [33]. Our primary aim was to systematically characterize CAF-specific membrane programs within the PDAC TME and to explore their potential roles in tumor progression and immune regulation. Based on these findings, we developed a CAF membrane–based prognostic signature (PaFMS) and evaluated its clinical relevance across multiple independent cohorts. Through this integrative transcriptomic framework, we sought to provide both a biologically informed view of CAF heterogeneity and a clinically relevant model for prognosis and therapeutic response prediction in PDAC.

Methods

Data collection

To comprehensively investigate the transcriptomic landscape of PDAC TME, we integrated multiple publicly available datasets. Three scRNA-seq cohorts: GSE154778 ($n = 16$), GSE197177 ($n = 8$), and GSE212966 ($n = 9$) were retrieved from the Gene Expression Omnibus (GEO) database (Supplementary table S1). For spatial transcriptomics analysis, two PDAC tumor samples (GSM6132061 and GSM6132063) from the GEO dataset GSE202740 were included (Supplementary table S2). Moreover, bulk RNA-seq data were compiled from several independent PDAC cohorts, including TCGA-PAAD (n = 146), ICGC-PACA-AU ($n = 91$), and five GEO datasets: GSE71729 ($n = 125$), GSE21501 ($n = 102$), GSE57495 ($n = 63$), GSE62452 ($n = 66$), and GSE78229 ($n = 49$). Corresponding clinical information is provided in Supplementary tables S3. According to the descriptions provided in the original studies, the spatial transcriptomics samples were derived from primary PDAC tumors from patients without prior anticancer treatment or other malignancy history [33]. For the scRNA-seq datasets, "PDAC primary" refers to samples obtained from primary PDAC tumor tissues, "liver metastases" refers to metastatic lesions of PDAC in the liver, and "adjacent normal" refers to pancreatic tissues adjacent to PDAC tumors or normal pancreatic tissues as defined in the original datasets [30, 34].

Furthermore, to explore the clinical relevance of identified molecular signatures in an immunotherapy context, we incorporated the IMvigor210 cohort, which includes detailed clinical information and transcriptomic data from 298 metastatic urothelial carcinoma patients treated with anti-PD-L1 therapy [36]. This dataset was accessed through the IMvigor210CoreBiologies R package.

Data processing and analysis

Single-cell RNA-seq data were processed following the standard Seurat pipeline [37]. For quality control, only cells with $1{,}000 < \text{nCount} < 100{,}000$, $500 < \text{nFeature} < 10{,}000$, and mitochondrial gene percentage (pMT) < 10% were retained. Data were normalized using the SCTransform function, followed by dimensionality reduction using RunPCA. To mitigate batch effects across samples, we applied the Harmony algorithm [38]. Next, uniform manifold approximation and projection (UMAP) was employed for visualization. Clustering was then performed using the FindNeighbors and FindClusters functions for downstream analyses.

Spatial transcriptomic data were normalized and spatially clustered using the BayesSpace [39] package. For bulk RNA-seq datasets, gene identifiers were first converted to gene symbols. For genes with multiple entries sharing the same symbol, expression values were averaged to obtain the final expression level. Odds ratios (ORs) were calculated to assess single-cell tissue preference.

Cell type annotation

Following Seurat analysis, a total of 25 single-cell clusters were identified and annotated based on previously reported marker genes and information from the CellMarker 2.0 database [40]. A total of 87,849 cells were classified into 8 major cell types. The marker genes used for annotation include PTPRC for immune cells; CD3E, CD3D and *NKG7* for T/NK cells; *CD79A*, *MS4A1*, *IGLC2* and *IGHA1* for B/plasma cells; *CD1C* for dendritic cells; *CD68*, *CD14* and *MACRO* for macrophages/monocytes; *CPA3* and *KIT* for Mast cells; *COL1A1* and *FAP* for fibroblasts; *PECAM1* and *VWF* for endothelial cells; and *EPCAM* and *KRT18* for epithelial cells.

Within the fibroblast population, 7 distinct subclusters were identified through re-dimensionality reduction and clustering. To determine the specific fibroblast subtypes represented by each cluster, we referred to previously reported marker genes [41], including *IL6*, *PDGFRA*, *CXCL12*, *CFD*, and *CXCL1* for iCAFs; *HLA-B* and *CD74* for apCAFs; and *ACTA2*, *MMP11*, *MYL9*, *HOPX*, and *TPM1* for myoCAFs.

Identification of PDAC CAF-specific gene signatures

To identify genes specifically upregulated in the myoCAF-c1 cluster compared to other fibroblast subpopulations, differential expression analysis was conducted using the FindAllMarkers function in Seurat. The Wilcoxon rank-sum test was applied (test.use = "wilcox"), and filtering parameters were set to include only positively regulated genes (only.pos = TRUE) with a minimum log2 fold change of 0.25 (logfc.threshold = 0.25) and expression in at least 25% of cells (min.pct = 0.25). The results of the differential expression analysis are provided in Supplementary table S4. Genes significantly enriched in the myoCAF-C1 cluster were subsequently visualized through volcano plots generated using the EnhancedVolcano package.

Differential expression genes (DEGs) analysis between the high-risk and low-risk groups in the TCGA-PAAD cohort was performed using the DESeq2 package. Based on the DEGs' results, functional enrichment analysis was subsequently conducted.

Cell trajectory and pseudotime analysis

Cellular differentiation trajectories were reconstructed using the monocle2 R package [42]. To ensure the reliability of dynamic gene expression modeling, genes with an average expression level below 0.1 were excluded from the analysis. Subsequently, genes exhibiting significant expression variability across cells were selected and used to order cells along a pseudotime axis. Dimensionality reduction was performed using the discriminative dimensionality reduction with trees (DDRTree) algorithm to facilitate trajectory inference. Pseudotime analysis was then conducted to identify key genes associated with cellular transitions. Cells located on the same trajectory branch were interpreted as occupying similar differentiation states.

Cell–cell communication analysis

Intercellular communication among different cell types was analyzed using CellChat [43]. CellChat predicts potential cell–cell interactions by integrating gene expression data with a curated database of known ligand–receptor and cofactor pairs. Following the standard workflow, cell–cell communication networks were independently inferred for each sample tissues. Normalized count matrices were used to construct CellChat objects, with CellChatDB.human selected as the reference database. All recommended preprocessing functions were applied, and analyses were performed with default parameters. The resulting CellChat objects from different tissues were then merged for comparative analysis. Communications involving fewer than 10 cells were excluded to ensure reliability. Visualization of the inferred interaction networks was performed using the built-in CellChat plotting functions and the ggplot2 R package.

Spatial transcriptomics analysis and feature enhancement

Following spatial clustering, each spot on the tissue section was annotated to one or more predominant cell types using the same panel of marker genes employed in the single-cell transcriptomic classification. To refine spatial resolution and improve spot-level cell type delineation, the spatialEnhance function from the BayesSpace package was applied [39]. Furthermore, spatial gene expression patterns related to tumor identity, CAFs-specific membrane genes, and pancreatic cancer-associated fibroblast membrane signature (PaFMS) were further accentuated using the enhanceFeatures function. A complete list of genes comprising these molecular signatures is provided in Supplementary table S5. To investigate spatial co-expression patterns, Pearson correlation analyses were conducted between enhanced features, and the resulting correlation matrices were visualized using the ggplot2 package.

PPI network construction and analysis

A protein–protein interaction (PPI) network was constructed for 33 identified myoCAF-c1 related membrane proteins using the STRING database, with the species restricted to

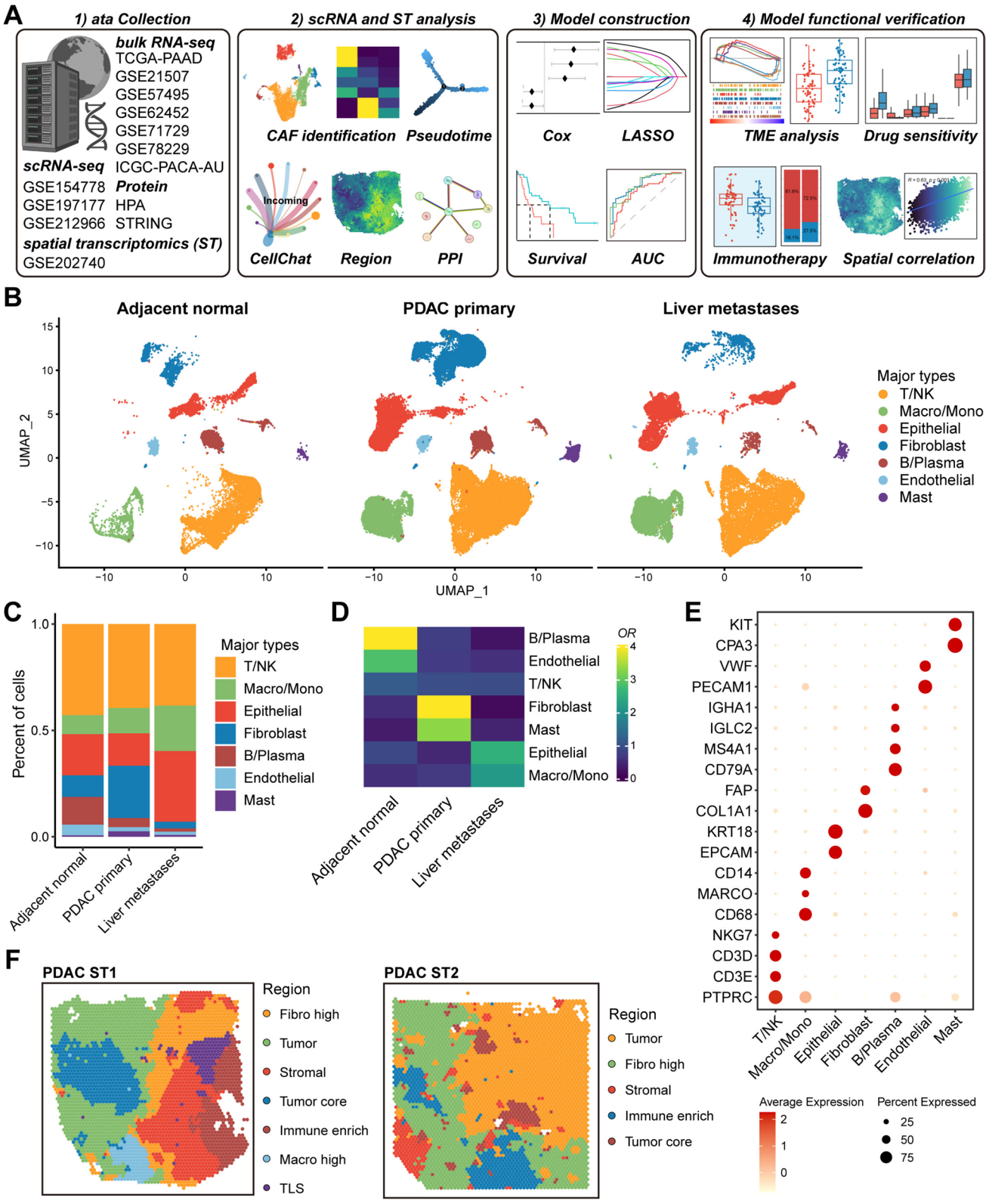

"Homo sapiens" and all other settings maintained at default values. To further explore the biological relevance of these interactions, functional pathway enrichment analysis was performed based on the PPI network, and the enriched pathways were visualized using the ggplot2 package for intuitive graphical representation.

◂**Fig. 1** Single-cell and spatial transcriptome landscapes of PDAC (**A**) Schematic of this study. (1) Datasets were obtained from GEO, TCGA, ICGC, HPA and STRING databases. (2) Single-cell RNA sequencing and spatial transcriptomics analysis revealed CAF-associated membrane genes. (3) The prognostic model was constructed based on the TCGA-PAAD cohort and evaluated using independent external datasets. (4) Functional analysis of prognostic model and verification of model signature genes. (**B**) UMAP plot of 7 main cell types colored by cell type identity, split by tissue types. Adjacent normal (15,089 cells); PDAC primary (47,942 cells); liver metastases (27,918 cells) (**C**) Proportion of cell types detected from adjacent normal (n = 4), PDAC primary (n = 19) and liver metastases (n = 10) tissues. (**D**) Heatmap showing the ORs of cell types occurring in each tissue. OR > 1.5 indicates that cell types are preferred to distribute in the corresponding tissue. (**E**) Dot plot showing the expression of cell specific marker genes across all cell types. (**F**) Spatial plot showing the annotation of 2 PDAC samples, each spot was annotated according to its major cellular composition. PDAC ST1, 3,794 spots; PDAC ST2, 3,217 spots

Construction and validation of the prognostic model PaFMS

A prognostic risk model was developed using transcriptomic and clinical data from the TCGA-PAAD cohort. Initially, 33 PDAC CAFs-specific membrane genes were identified from scRNA-seq analyses. To assess their prognostic relevance, univariate Cox proportional hazards regression was performed. Genes with a p-value < 0.05 and a hazard ratio (HR) significantly different from 1 were considered statistically significant and retained for subsequent modeling to minimize the risk of overfitting.

To refine the prognostic gene set, least absolute shrinkage and selection operator (LASSO) regression was employed. Model optimization was achieved through ten-fold cross-validation, and genes with non-zero regression coefficients were selected. The PaFMS was established using the expression values and corresponding coefficients of these genes (Supplementary table S6). Patients were stratified into high- and low-risk groups based on the median PaFMS score. The PaFMS score was calculated using the following formula:

$$PaFMS = \sum_{i=1}^{k} risk\ coefficient(i) * mRNA\ expression(i)$$

The prognostic utility of the PaFMS signature was assessed using Kaplan–Meier survival analysis, with statistical significance determined by the log-rank test. Time-dependent receiver operating characteristic (ROC) curves were generated to evaluate predictive accuracy at different time points, and the corresponding area under the curve (AUC) values were computed using the timeROC package in R. To confirm the robustness and generalizability of the PaFMS model, external validation was conducted using multiple independent PDAC cohorts obtained from the ICGC and GEO databases.

Functional analysis of myoCAF-c1 and PaFMS signature

KEGG and HALLMARK gene sets were obtained from the Molecular Signatures Database (MSigDB). For each fibroblast subcluster, single-sample gene set enrichment analysis (ssGSEA) was conducted across all 50 HALLMARK pathways using the "ssgsea" method implemented in the GSVA package.

For the PaFMS, patients were divided into high- and low-risk groups based on calculated risk scores. DEGs analysis was conducted between the two groups, and genes were ranked by fold change. Subsequently, gene set enrichment analysis (GSEA) based on KEGG pathways was carried out using the fgsea package in R. Significantly upregulated and downregulated pathways were selected for visualization.

Tumor microenvironment and infiltration analysis

To investigate the correlation between the PaFMS risk score and PDAC TME composition, stromal and immune cell infiltration levels were quantified using the ESTIMATE and CIBERSORT algorithms [44]. Patients were classified into high- and low-risk groups according to the median PaFMS score. Comparative analysis of infiltration scores between groups was conducted using the Wilcoxon rank-sum test. Visualization of the immune and stromal landscape, derived respectively from ESTIMATE and CIBERSORT results, was performed using the ggplot2 package in R.

Prediction of therapeutic response

To explore the potential correlation between PaFMS risk scores and sensitivity to anticancer agents, we applied the pRRophetic [45] R package (version 0.5) to predict drug responses based on the mRNA expression profiles of tumor samples from the TCGA-PAAD cohort. Drug sensitivity estimation was performed using the pRRopheticPredict function, with parameters set to tissueType = "solid" and dataset = "cgp2014". A total of 138 compounds were assessed across the cohort. Comparative analyses were conducted between the high- and low-risk groups defined by PaFMS scores. Predicted differences in drug sensitivity were visualized using boxplots generated via the ggboxplot function from the ggpubr package. A summary of statistically significant drug-risk group associations is provided in Supplementary table S7.

Protein expression of PaFMS signature

To assess the protein-level expression of PaFMS signature genes, immunohistochemistry (IHC) data for four representative membrane proteins were obtained from the Human Protein Atlas (HPA; https://www.proteinatlas.org/). Representative IHC

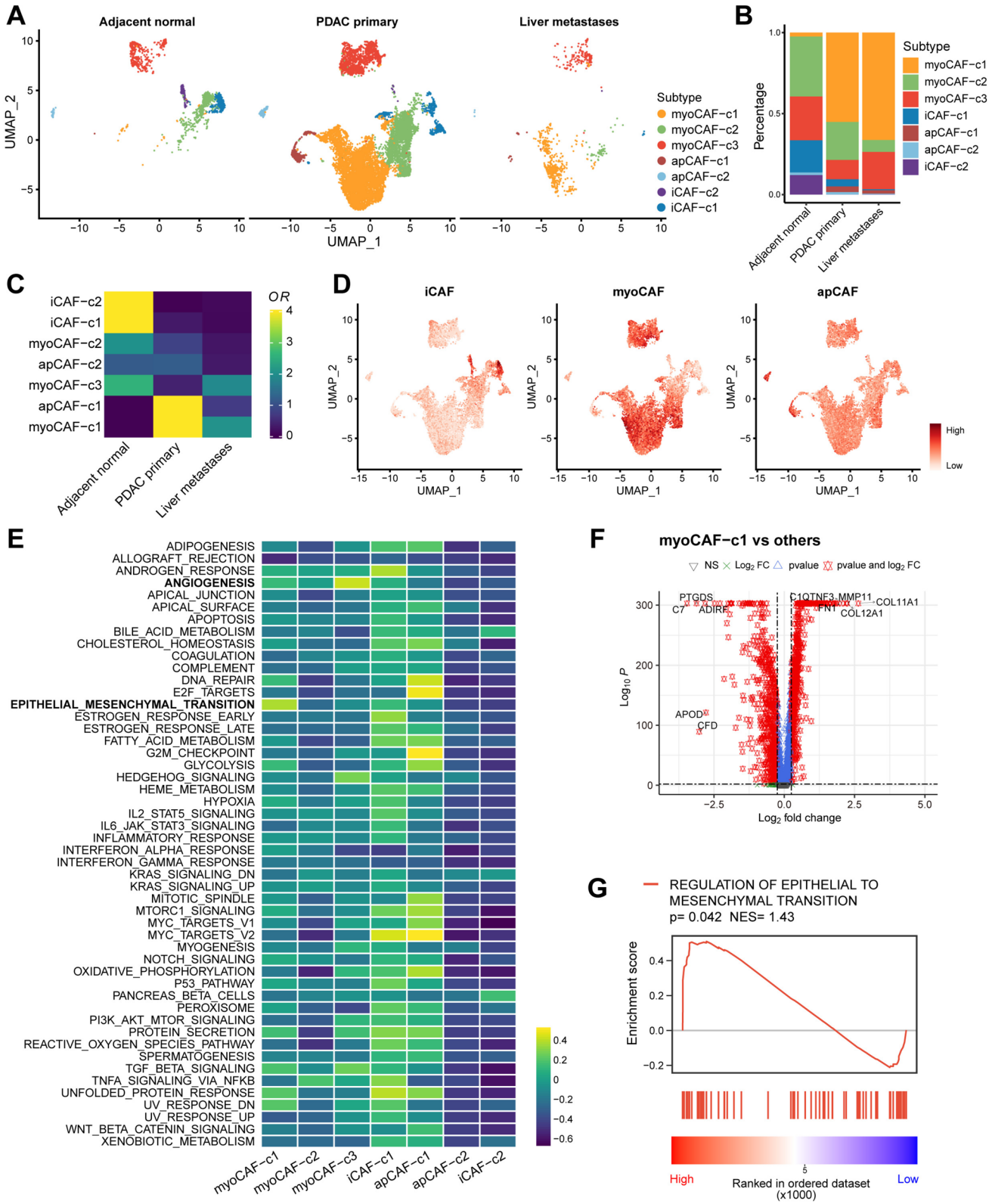

images from PDAC tissues, liver cancer tissues, and matched normal pancreatic tissues were analyzed. Due to the unavailability of protein expression data for *IGFBP3* in the HPA, this gene was excluded from visualization. In the HPA, protein staining intensity is categorized into four levels: "not detected", "low", "medium", and "high".

◂**Fig. 2** Identification of tumor-specific fibroblast clusters in PDAC primary tissues. (**A**) UMAP plot of 7 main fibroblast clusters colored by cell type identity, split by tissue types. Adjacent normal (1,434 cells); PDAC primary (11,001 cells); liver metastases (683cells). (**B**) Proportion of fibroblast clusters detected from adjacent normal, PDAC primary and liver metastases tissues. (**C**) Heatmap showing the ORs of cell clusters occurring in each tissue. (**D**) Feature plot of fibroblast subtype marker genes expression in all fibroblasts. Feature plots were generated based on the AddModuleScore function. (**E**) Heatmap showing the ssGSEA score of 50 hallmark pathways across 7 fibroblast clusters. (**F**) Volcano plot showing the DEGs between myoCAF-c1 and other cell clusters in fibroblasts. (**G**) GSEA plot showing the upregulation of regulation of epithelial mesenchymal transition pathway in myoCAF-c1 cells

Statistical analysis

Group comparisons were performed using either Student's t-test or the Wilcoxon rank-sum test, depending on data normality and distribution. Overall survival differences were assessed using the log-rank test. A two-sided p-value < 0.05 was considered statistically significant. Significance levels were indicated as follows: $*p < 0.05$, $**p < 0.01$, and $***p < 0.001$.

Results

Single-cell and spatial transcriptome landscapes of PDAC TME

This study integrated scRNA-seq, spatial transcriptomics, and bulk RNA-seq data from publicly databases to systematically identify PDAC CAFs-specific membranes (Fig. 1A). These membranes were further used for prognostic model construction and therapeutic response prediction (Fig. 1A). We initially analyzed a total of 31 scRNA-seq samples from three independent datasets, comprising 19 PDAC primary

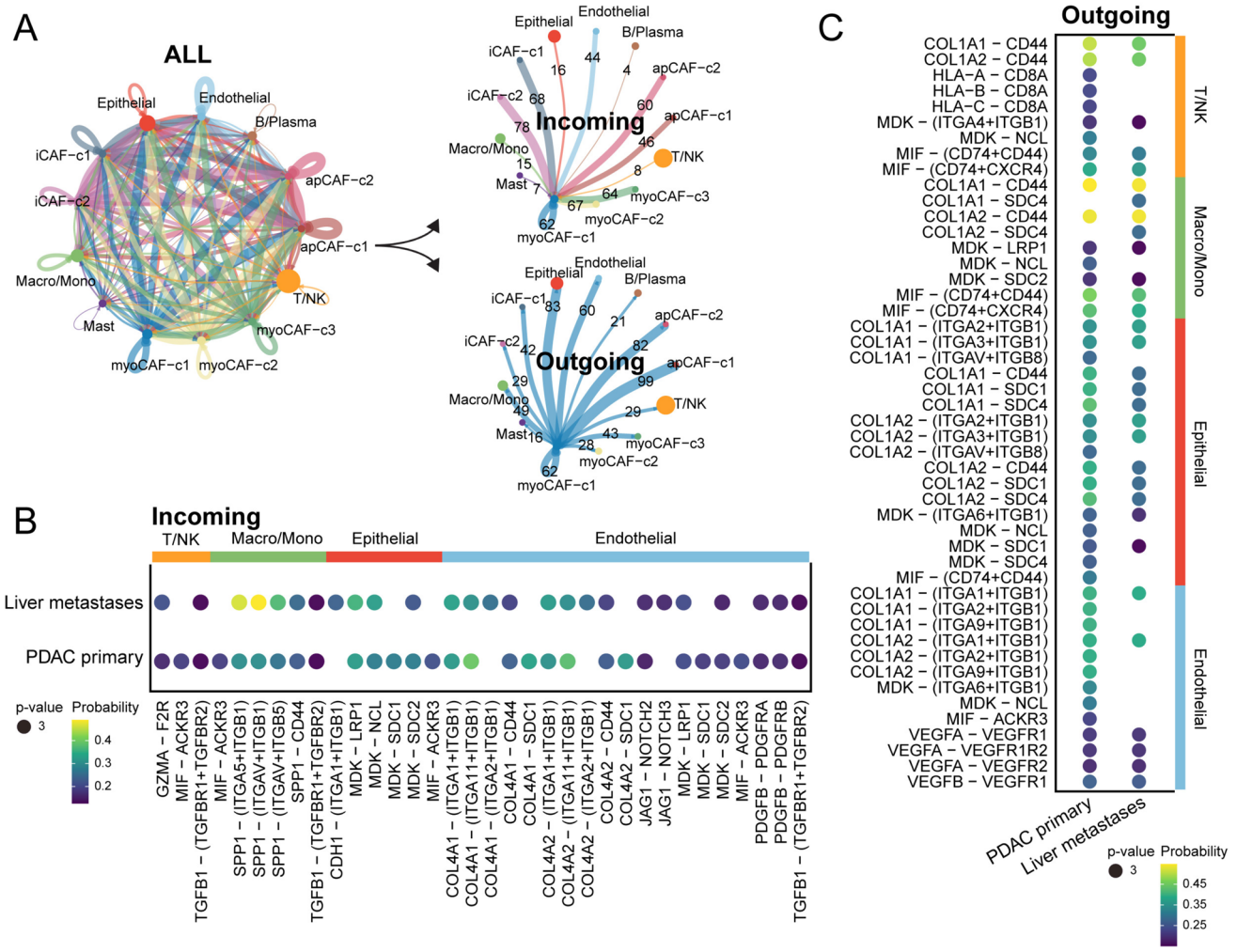

Fig. 3 Cell–cell communication analysis between myoCAF-c1 and others. (**A**) Interaction network of main cell types constructed with CellChat. (**B**) Bubble plot of predicted incoming interactions between myoCAF-c1 and four cell types in the TME. (**C**) Bubble plot of predicted outgoing interactions between myoCAF-c1 and four cell types in the TME

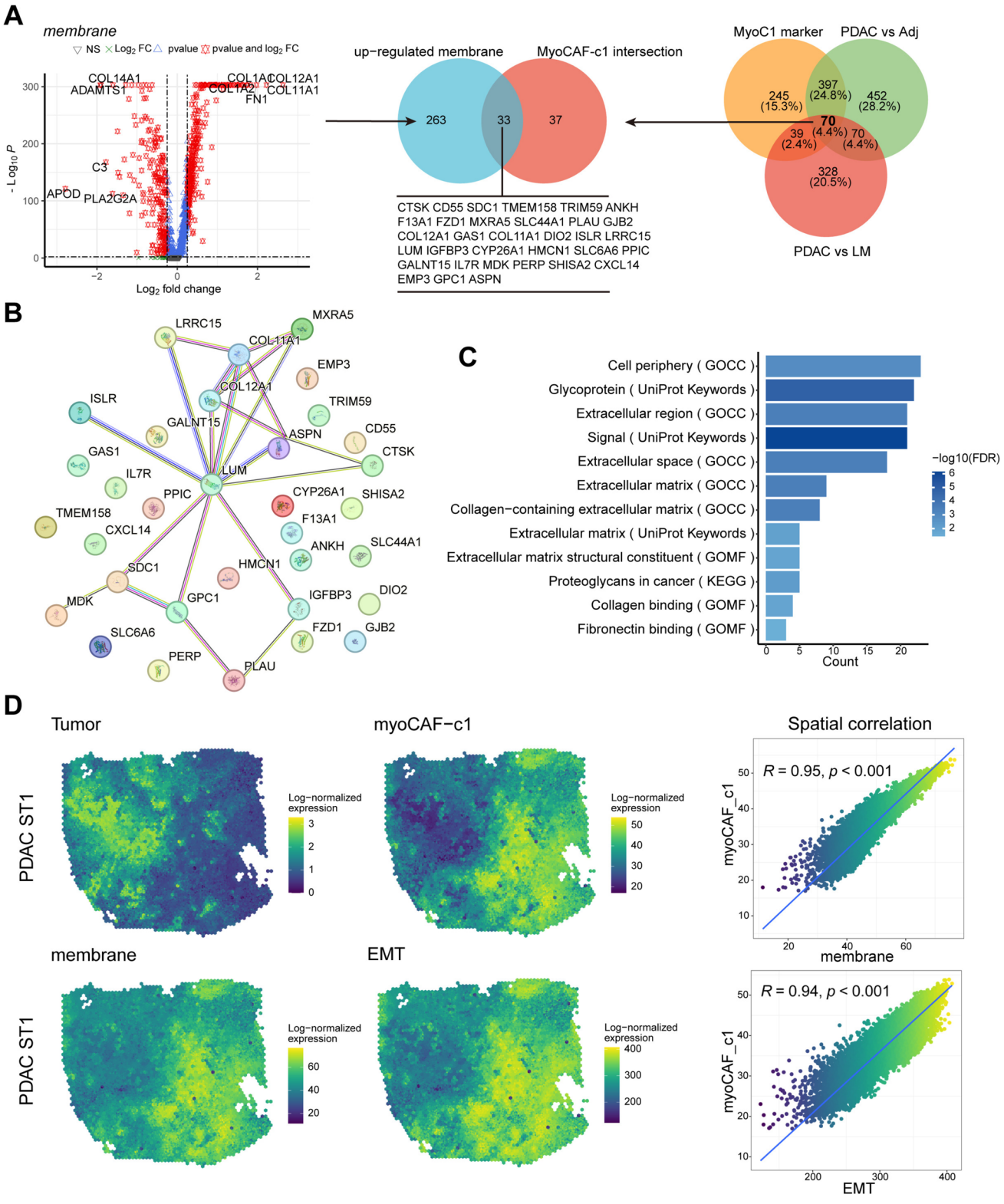
A
membrane
NS Log2 FC pvalue pvalue and log2 FC
COL14A1
ADAMTS1
COL1A1
COL12A1
COL1A2
COL11A1
FN1
C3
APOD
PLA2G2A
- Log10 P
Log2 fold change
up−regulated membrane
MyoCAF-c1 intersection
263
33
37
CTSK CD55 SDC1 TMEM158 TRIM59 ANKH
F13A1 FZD1 MXRA5 SLC44A1 PLAU GJB2
COL12A1 GAS1 COL11A1 DIO2 ISLR LRRC15
LUM IGFBP3 CYP26A1 HMCN1 SLC6A6 PPIC
GALNT15 IL7R MDK PERP SHISA2 CXCL14
EMP3 GPC1 ASPN
MyoC1 marker
PDAC vs Adj
245 (15.3%)
397 (24.8%)
452 (28.2%)
70
39 (2.4%)
(4.4%)
70 (4.4%)
328 (20.5%)
PDAC vs LM
B
LRRC15
MXRA5
COL11A1
EMP3
COL12A1
ISLR
TRIM59
GALNT15
ASPN
CD55
GAS1
CTSK
IL7R
LUM
PPIC
CYP26A1
SHISA2
TMEM158
F13A1
CXCL14
ANKH
SLC44A1
SDC1
HMCN1
MDK
GPC1
IGFBP3
DIO2
SLC6A6
FZD1
GJB2
PERP
PLAU
C
Cell periphery (GOCC)
Glycoprotein (UniProt Keywords)
Extracellular region (GOCC)
Signal (UniProt Keywords)
Extracellular space (GOCC)
Extracellular matrix (GOCC)
Collagen−containing extracellular matrix (GOCC)
Extracellular matrix (UniProt Keywords)
Extracellular matrix structural constituent (GOMF)
Proteoglycans in cancer (KEGG)
Collagen binding (GOMF)
Fibronectin binding (GOMF)
Count
−log10(FDR)
D
Tumor
myoCAF−c1
Spatial correlation
PDAC ST1
Log−normalized expression
R = 0.95, p < 0.001
myoCAF_c1
membrane
membrane
EMT
PDAC ST1
Log−normalized expression
R = 0.94, p < 0.001
myoCAF_c1
EMT

◂**Fig. 4** Characterization of PDAC myoCAF-c1 specific membranes. (**A**) Volcano plot showing the differential expression of membrane-associated genes between myoCAF-c1 and other cell clusters in fibroblasts (Left). The intersection of up-regulated membrane-associated genes and myoCAF-c1 related DEGs in PDAC (Middle). Venn plot showing the intersection of myoCAF-c1 marker genes and up-regulated genes in PDAC versus Adjacent/LM sites (Right). (**B**) The protein–protein interaction (PPI) network of 33 myoCAF-c1 related membrane proteins using STRING online database. (**C**) Bar plot showing the functional enrichment of gene ontology (GO), KEGG and UniPort Keywords pathways associated with 33 myoCAF-c1 related membrane proteins within panel (B). (**D**) Spatial distribution of tumor, myoCAF-c1 spatial signature score, membrane and EMT genes in PDAC ST1 sample. (**E**) The correlation between membrane, EMT and myoCAF-c1 spatial signature score in PDAC ST1 sample

tissues, 4 adjacent normal tissues, and 10 liver metastases tissues (Supplementary table S1). Following rigorous quality control procedures, 87,949 high-quality cells were retained for downstream analysis (Fig. S1A-B). Principal component analysis (PCA), batch effect correction, and dimensionality reduction and clustering were subsequently performed, leading to the identification of 25 distinct cellular clusters. Based on canonical marker gene expression, these clusters were annotated into different cell types (Fig. S1C-D). After filtering out the "ambiguous" cells, seven major cell lineages were retained for downstream analysis (Fig. 1B). Comparative analysis of cellular composition across tissue types revealed a significant enrichment of fibroblasts in PDAC primary tumors, whereas macrophages/monocytes and epithelial cells were predominantly increased in liver metastases (Fig. 1C). These trends were further validated by single-cell tissue preference analysis using odds ratios (OR) (Fig. 1D). Expression of representative marker genes demonstrated cell type-specific patterns (Fig. 1E). For instance, *COL1A1* and *FAP* were selectively expressed in fibroblasts, while *PTPRC* marked all immune cell populations (Fig. 1E). In addition, two spatial transcriptomics samples from PDAC tumors were analyzed (Fig. 1F). Spots were annotated using BayesSpace cluster results in combination with marker gene signatures (Fig. S1E-F). The spatial maps revealed a compartmentalized architecture in which fibroblast-enriched stromal regions were interposed between tumor areas and immune-infiltrated spots, suggesting a spatially organized tumor–stroma–immune interface (Fig. 1F). Collectively, these analyses delineated the cellular composition of PDAC and liver metastases, highlighting the enrichment of fibroblasts in primary tumors and the increased presence of macrophages/monocytes and epithelial cells in metastatic lesions. The spatial transcriptomics analysis further revealed an organized tumor–stroma–immune architecture, providing a cellular framework for subsequent identification of CAF-associated membrane proteins.

Characterization of PDAC cancer-associated fibroblast sub-cluster

To identify fibroblasts specifically enriched in PDAC primary tumors, we isolated a total of 13,118 fibroblast cells and performed clustering and subtype classification (Fig. 2A). All fibroblasts were annotated into three canonical CAF subtypes: myoCAFs, iCAFs, and apCAFs (Fig. S2A-B). Compared to adjacent normal tissues, the myoCAF-c1 subcluster accounted for a significantly higher proportion of fibroblasts in PDAC primary tissues (Fig. 2B). Further single-cell tissue preference analysis supported that myoCAF-c1 exhibited the highest OR in PDAC primary tissues rather than in liver metastases or adjacent normal tissues (Fig. 2C). We next visualized the module score of the three CAF subtypes (Fig. 2D). Top 5 genes for each CAF subcluster were identified, and the results showed COL11A1, MMP11 and COL12A1 were highly expressed within myoCAF-C1 cluster (Fig. S2C). Moreover, the HALLMARK pathway analysis indicated a notable enrichment of epithelial-mesenchymal transition (EMT) signaling in this myoCAF-c1 cluster (Fig. 2E). Notably, myoCAF-c1 and c3 were enriched in angiogenesis pathway, which may contribute to tumor proliferation. Subsequent differential expression analysis confirmed that COL11A1, MMP11, COL12A1, C1QTNF3, and FN1 were significantly upregulated in the myoCAF-c1 subcluster compared to other fibroblast clusters (Fig. 2F). Furthermore, GSEA analysis demonstrated myoCAF-C1 upregulated genes significant enriched in the regulation of EMT ($p = 0.042$, NES = 1.43) and focal adhesion ($p = 2e\text{-}4$, NES = 1.84) in the myoCAF-c1 cluster (Fig. 2G, S2D). we also investigated the differentiation dynamics of those fibroblast subpopulations (Fig. S2E-G). When pseudotime was ordered from normal to tumor states (Fig. S2F), myoCAF-c1 cluster cells were predominantly positioned within the primary PDAC tissues, suggesting that they may originate from normal fibroblasts and differentiate into tumor-associated fibroblasts along this trajectory. These findings indicated that myoCAF-c1 represents an EMT-associated CAF population predominantly enriched in PDAC primary compared with adjacent normal and liver metastases tissues.

Interactions of myoCAF-c1 with tumor and tumor progression–associated cells

Given the association of myoCAF-c1 with epithelial–mesenchymal transition (EMT) and angiogenesis, we further investigated intercellular communications involving this subtype. myoCAF-c1 exhibited extensive interactions with multiple

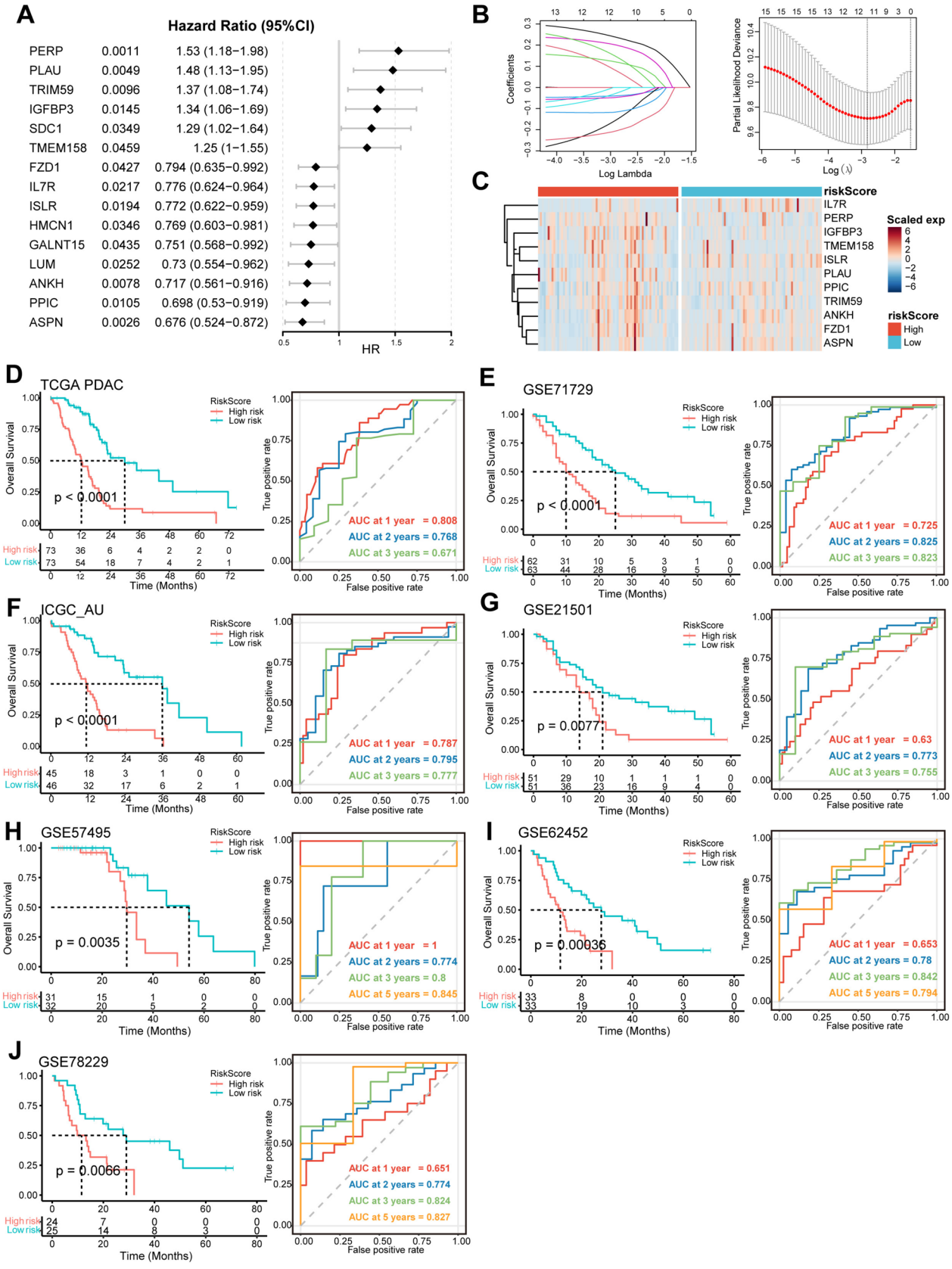
A
Hazard Ratio (95%CI)
PERP 0.0011 1.53 (1.18−1.98)
PLAU 0.0049 1.48 (1.13−1.95)
TRIM59 0.0096 1.37 (1.08−1.74)
IGFBP3 0.0145 1.34 (1.06−1.69)
SDC1 0.0349 1.29 (1.02−1.64)
TMEM158 0.0459 1.25 (1−1.55)
FZD1 0.0427 0.794 (0.635−0.992)
IL7R 0.0217 0.776 (0.624−0.964)
ISLR 0.0194 0.772 (0.622−0.959)
HMCN1 0.0346 0.769 (0.603−0.981)
GALNT15 0.0435 0.751 (0.568−0.992)
LUM 0.0252 0.73 (0.554−0.962)
ANKH 0.0078 0.717 (0.561−0.916)
PPIC 0.0105 0.698 (0.53−0.919)
ASPN 0.0026 0.676 (0.524−0.872)
HR
B
Coefficients
Log Lambda
Partial Likelihood Deviance
Log (λ)
C
riskScore
IL7R
PERP
IGFBP3
TMEM158
ISLR
PLAU
PPIC
TRIM59
ANKH
FZD1
ASPN
Scaled exp
riskScore
High
Low
D
TCGA PDAC
RiskScore
High risk
Low risk
Overall Survival
p < 0.0001
High risk 73 36 6 4 2 2 0
Low risk 73 54 18 7 4 2 1
Time (Months)
True positive rate
False positive rate
AUC at 1 year = 0.808
AUC at 2 years = 0.768
AUC at 3 years = 0.671
E
GSE71729
p < 0.0001
High risk 62 31 10 5 3 1 0
Low risk 63 44 28 16 9 5 0
AUC at 1 year = 0.725
AUC at 2 years = 0.825
AUC at 3 years = 0.823
F
ICGC_AU
p < 0.0001
High risk 45 18 3 1 0 0
Low risk 46 32 17 6 2 1
AUC at 1 year = 0.787
AUC at 2 years = 0.795
AUC at 3 years = 0.777
G
GSE21501
p = 0.0077
High risk 51 29 10 1 1 1 0
Low risk 51 36 23 16 9 4 0
AUC at 1 year = 0.63
AUC at 2 years = 0.773
AUC at 3 years = 0.755
H
GSE57495
p = 0.0035
High risk 31 15 1 0 0
Low risk 32 20 5 2 0
AUC at 1 year = 1
AUC at 2 years = 0.774
AUC at 3 years = 0.8
AUC at 5 years = 0.845
I
GSE62452
p = 0.00036
High risk 33 8 0 0 0
Low risk 33 19 10 3 0
AUC at 1 year = 0.653
AUC at 2 years = 0.78
AUC at 3 years = 0.842
AUC at 5 years = 0.794
J
GSE78229
p = 0.0066
High risk 24 7 0 0 0
Low risk 25 14 8 3 0
AUC at 1 year = 0.651
AUC at 2 years = 0.774
AUC at 3 years = 0.824
AUC at 5 years = 0.827

◂**Fig. 5** Identification of risk genes and construction of PaFMS. (**A**) Forest plot of COX analysis showing 15 myoCAF-c1 related membrane-associated genes significantly associated with prognosis of PDAC samples. (**B**) LASSO analysis identifying prognostic membrane-associated genes. (**C**) Heatmap showing the expression of 9 signatures in high and low-risk samples. (**D**) Survival analysis of high- and low-risk samples and ROC analysis results at 1, 2, and 3 years in the TCGA PDAC dataset (**E-J**) Survival analysis of high- and low-risk samples and ROC analysis results in GSE71729 (E), ICGC_AU (**F**), GSE21501 (**G**), GSE57495 (**H**), GSE62452(**I**) and GSE78229 (**J**)

cell types (Fig. 3A). We defined interactions received by or originating from myoCAF-c1 as incoming and outgoing signals, respectively. myoCAF-c1 received inputs primarily from endothelial (44), epithelial (16), macrophage/monocyte (15), and T/NK (8) cells, while transmitting outgoing signals toward epithelial (83), endothelial (60), macrophage/monocyte (49), and T/NK (29) populations (Fig. 3A).

We next compared signaling interactions within the TME of primary PDAC and liver metastases (Fig. 3B–C). In primary PDAC, myoCAF-c1 presented HLA molecules to T/NK cells and was targeted by T/NK cell cytotoxicity via the GZMA–F2R axis. Midkine (MDK) signaling was shared between myoCAF-c1 and multiple cell types, with the MDK–NCL interaction consistently detected across four major cell populations in primary PDAC. myoCAF-c1 and macrophage/monocyte cells primarily communicated through COLLAGEN and MIF signaling, with strong probabilities observed in both primary and metastatic sites. Moreover, macrophage/monocyte cells regulated myoCAF-c1 via the SPP1–integrin pathway, which was more active in liver metastases than in primary PDAC. We also found that myoCAF-c1 promoted endothelial proliferation via VEGF signaling, while endothelial cells, in turn, enhanced myoCAF-c1 activation through COL4A1/2, NOTCH, and PDGF signaling. Notably, $COL4A1^{+}$ endothelial cells have been identified as tumor-associated endothelium [14], consistent with our observations. Collectively, these results highlight the critical role of myoCAF-c1 in shaping both primary and metastatic PDAC TMEs, potentially driving tumor progression and dissemination through EMT and angiogenesis.

Identification of PDAC CAF-specific membrane genes

Membrane proteins are critical mediators of cell–cell communication, signaling, and therapeutic targeting in cancers [25, 46, 47]. We first identified 299 membrane genes upregulated in myoCAF-c1 compared with other fibroblast subtypes. To delineate PDAC-specific myoCAF-c1 signatures, we next integrated three expression contrasts—primary PDAC versus adjacent normal fibroblasts, primary PDAC versus liver metastasis fibroblasts, and myoCAF-c1 versus other fibroblasts—to derive a core PDAC myoCAF-c1 gene set. Cross-referencing this set with myoCAF-c1–enriched membrane genes yielded 33 definitive candidates, including *CTSK*, *CD55*, *SDC1*, *TMEM158*, and *TRIM59* (Fig. 4A). Furthermore, PPI network revealed a dense interaction landscape among these PDAC myoCAF-c1 specific membrane proteins, with LUM serving as a hub node directly connected to multiple ECM-related genes such as *COL11A1*, *ASPN*, and *SDC1* (Fig. 4B). Functional enrichment analysis of the PPI network highlighted significant enrichment in extracellular matrix organization and other membrane-associated pathways (Fig. 4C).

To explore their spatial localization within the PDAC TME, spatial transcriptomic mapping was performed for myoCAF-c1 marker genes, and the 33 membrane genes, EMT-related genes, and the epithelial marker *EPCAM*. The spatial maps demonstrated that myoCAF-c1 marker genes did not spatially colocalize with tumor cells but exhibited strikingly similar distribution patterns to EMT regions, implying a functional role of myoCAF-c1 in EMT activation (Fig. 4D, S3A-C). Correlation analyses showing positive associations between myoCAF-c1 marker genes and EMT regions (sample ST1: $R = 0.95$, $p < 0.001$; sample ST2: $R = 0.81$, $p < 0.001$), also between membrane genes and EMT regions (sample ST1: $R = 0.94$, $p < 0.001$; sample ST2: $R = 0.9$, $p < 0.001$) across both two spatial transcriptomic datasets (Fig. 4D, S3B-C). These findings suggest that PDAC myoCAF-c1 specific membrane genes hold substantial potential for further investigation in the context of pancreatic cancer and therapeutic development.

Identification of risk genes and construction of PaFMS

To evaluate the prognostic potential of PDAC myoCAF-c1 specific membrane genes, we first performed univariate Cox regression analysis of 33 candidate genes in the TCGA-PAAD cohort, identifying 15 genes significantly associated with overall survival (Fig. 5A). These genes were further analyzed using LASSO-Cox regression with the minimum λ criterion, yielding 11 genes with non-zero coefficients for the construction of PaFMS model (Fig. 5B, Table S5). Patients were stratified into high- and low-risk groups based on the median PaFMS risk score. Among the 11 model genes, *PERP*, *PLAU*, *IGFBP3*, *TRIM59*, and *TMEM158* showed markedly higher expression in the high-risk group (Fig. 5C). Survival analysis revealed that patients with high PaFMS scores had significantly worse outcomes (log-rank $p < 0.0001$), and time-dependent ROC curves demonstrated robust predictive accuracy, with AUCs of 0.808, 0.768, and 0.617 for 1-, 2-, and 3-year overall survival (OS)

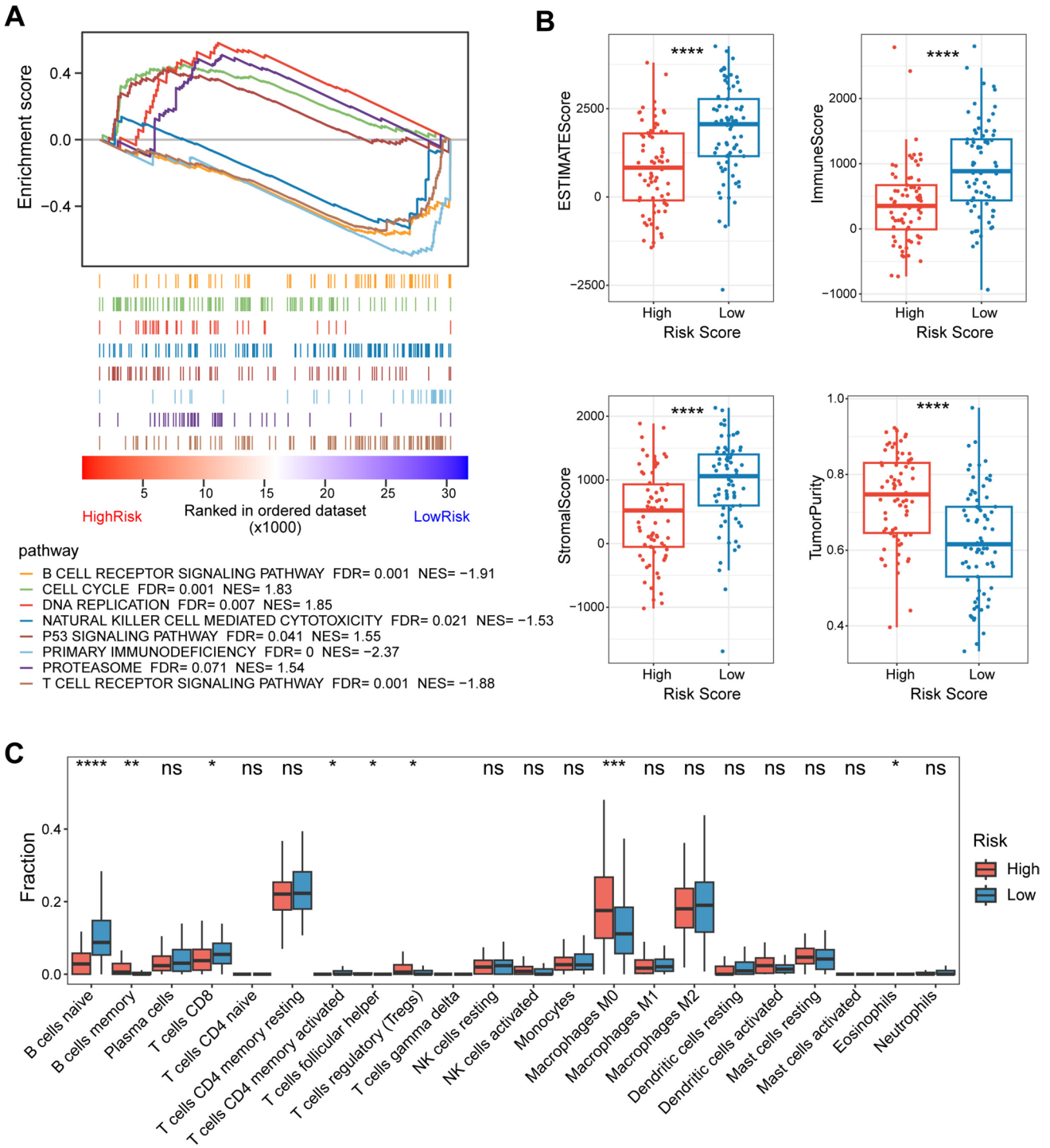

Fig. 6 Functional enrichment analysis and infiltration of immune cells in PaFMS. (**A**) GSEA plot showing the up-regulated and down-regulated KEGG pathways in high- and low-risk groups based on the TCGA dataset. (**B**) Boxplot showing the difference of ESTIMATE score, immune score, stromal score, and tumor purity in high- and low-risk groups. (**C**) Boxplot showing the immune cell infiltrating results via CIBERSORT based on the TCGA dataset

in the TCGA cohort, respectively (Fig. 5D). Importantly, the prognostic predictive value of PaFMS was consistently validated across six independent external cohorts, including GSE71729 (log-rank $p < 0.0001$; AUCs of 0.725, 0.825, and 0.823 for 1-, 2-, and 3-year OS; Fig. 5E), ICGC-AU (log-rank $p < 0.0001$; AUCs of 0.787, 0.795, and 0.777 for 1-, 2-, and 3-year OS; Fig. 5F), GSE21501 (log-rank p = 0.0077; AUCs of 0.63, 0.773, and 0.755 for 1-, 2-, and 3-year OS;

Fig. 5G), GSE57495 (log-rank $p = 0.0035$; AUCs of 1, 0.774, 0.8 and 0.845 for 1-, 2-, 3- and 5-year OS; Fig. 5H), GSE62452 (log-rank $p = 0.00036$; AUCs of 0.653, 0.78, 0.842 and 0.794 for 1-, 2-, 3- and 5-year OS; Fig. 5I), and GSE78229 (log-rank $p = 0.0066$; AUCs of 0.651, 0.774, 0.824 and 0.827 for 1-, 2-, 3- and 5-year OS; Fig. 5J), collectively confirming its broad applicability. Thus, these results demonstrate that PaFMS is a robust prognostic indicator in PDAC, providing a potential framework for risk stratification and individualized treatment planning.

Enrichment of proliferative pathways and suppression of immune infiltration associated with high PaFMS scores

To explore the functional implications of the PaFMS, we performed DEGs analysis between the high- and low-risk groups. GSEA of the DEGs revealed that cell cycle (NES = 1.83), DNA replication (NES = 1.85), proteasome (NES = 1.54), and p53 signaling pathway (NES = 1.55) were significantly upregulated in the high-risk group, whereas immune-related pathways, including T cell receptor signaling (NES = −1.88), B cell receptor signaling (NES = −1.91), natural killer cell mediated cytotoxicity (NES = −1.53), and primary immunodeficiency (NES = −2.37) were markedly downregulated (Fig. 6A). These findings suggest that PaFMS may be negative associated with the immune response and infiltration of immune cells in the PDAC TME. To further investigate this relationship, we applied the ESTIMATE and CIBERSORT algorithms to assess immune and stromal cell infiltration in the TCGA-PAAD cohort. The ESTIMATE results demonstrated that the high-risk group exhibited lower ESTIMATE, immune, and stromal scores, but higher tumor purity compared with the low-risk group (Fig. 6B). Consistently, CIBERSORT analysis showed that the proportions of B cells and T cells were reduced in the high-risk group, while M0 macrophages were significantly enriched (Fig. 6C). Together, these results indicated that a higher PaFMS score is associated with impaired immune infiltration, thereby shedding light on the potential functional role of PaFMS in shaping the PDAC immune microenvironment.

PaFMS is associated with drug sensitivity and immunotherapy

To investigate the potential clinical relevance of PaFMS, we assessed the association between PaFMS risk groups and predicted sensitivity to anti-cancer agents using the Cancer Genome Project (CGP 2014) dataset. Based on the TCGA-PAAD transcriptomic profiles, the IC50 values of 138 compounds were estimated for PDAC patients. Comparative analysis revealed that IC50 values for 33 drugs differed significantly between the high- and low-risk groups (Table S7). Among these, 29 agents exhibited lower IC50 values in the low-risk group, whereas 4 agents showed lower IC50 values in the high-risk group (Fig. 7A). Notably, low-risk patients demonstrated significantly lower IC50 values for AKT inhibitor VIII ($p = 0.0038$), AZ628 ($p = 0.017$), Pazopanib ($p = 0.016$), and Parthenolide ($p = 0.046$), suggesting potential therapeutic benefit in this group. Conversely, Mitomycin C ($p = 0.046$), BI-2536 ($p = 0.033$), selumetinib (AZD6244; $p = 0.0011$), and PLX4720 ($p = 4.8 \times 10^{-5}$) exhibited lower IC50 values in the high-risk group, indicating possible preferential efficacy in these patients.

To further explore the role of PaFMS in immunotherapy, we analyzed the Imvigor210 cohort comprising patients treated with anti-PD-L1 therapy (Fig. 7B-E). Survival analysis confirmed the prognostic stratification ability of PaFMS in this immunotherapy cohort, which patients with high PaFMS score were associated with worse outcomes (log-rank p = 0.031; Fig. 7B). Moreover, patients responding to anti-PD-L1 treatment had significantly lower PaFMS scores compared with non-responders ($p = 0.03$; Fig. 7C). When stratified by median PaFMS score, the proportion of responders was higher in the low-risk group; however, this trend did not reach statistical significance ($p = 0.072$; Fig. 7D). Analysis of immune checkpoint expression revealed that *PD-1*, *PD-L1*, *CTLA4*, and *TIGIT* were all more highly expressed in the high-risk group, suggesting an immunosuppressive TME in these patients and potential suitability for immune checkpoint blockade (Fig. 7E). These findings suggest that PaFMS possesses predictive power for drug response and may help optimize personalized immunotherapy strategies for PDAC.

Expression characteristics of the PaFMS signature genes

To further validate the expression patterns of PaFMS signatures, we analyzed multiple transcriptomic datasets. scRNA-seq data demonstrated that these genes were predominantly expressed in PDAC primary tissues and, to a lesser extent, in liver metastases, while showing minimal expression in adjacent normal tissues (Fig. 8A). Notably, with the exception of *IL7R*, which was enriched in T/NK cells, and *PERP*, predominantly expressed in endothelial cells, most PaFMS genes exhibited fibroblast-specific expression (Fig. S4A). Within fibroblasts, these genes showed elevated expression not only in the myoCAF-c1 subcluster but also in myoCAF-c2, apCAF-c1, and iCAF-c2 populations (Fig. 8B). Building on this observation, we focused on four key genes with relatively high hazard ratios (Fig. 8A)—*PLAU*, *TMEM158*, *TRIM59*, and *IGFBP3*—and performed spatial transcriptomic analyses in two PDAC samples. The expression of these genes and PaFMS signature, spatially co-localized with myoCAF-c1 spatial regions, highlighting a strong spatial association between PaFMS genes (for example, *PLAU*:

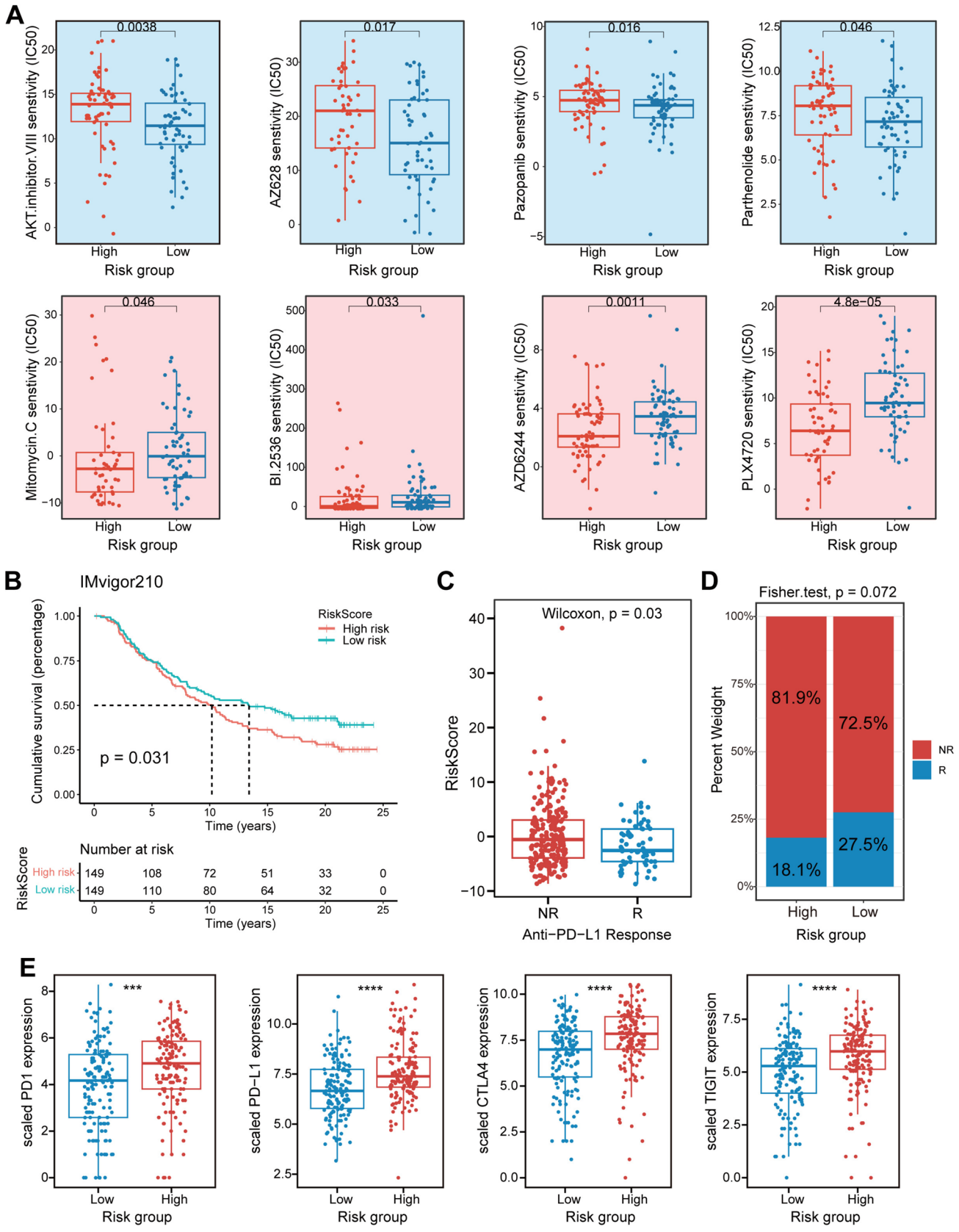
A
AKT.inhibitor.VIII senstivity (IC50)
0.0038
AZ628 senstivity (IC50)
0.017
Pazopanib senstivity (IC50)
0.016
Parthenolide senstivity (IC50)
0.046
Mitomycin.C senstivity (IC50)
0.046
BI.2536 senstivity (IC50)
0.033
AZD6244 senstivity (IC50)
0.0011
PLX4720 senstivity (IC50)
4.8e−05
High
Low
Risk group
B
IMvigor210
Cumulative survival (percentage)
RiskScore
High risk
Low risk
p = 0.031
Time (years)
Number at risk
High risk 149 108 72 51 33 0
Low risk 149 110 80 64 32 0
C
Wilcoxon, p = 0.03
RiskScore
NR
R
Anti−PD−L1 Response
D
Fisher.test, p = 0.072
Percent Weidght
81.9%
72.5%
18.1%
27.5%
NR
R
E
scaled PD1 expression
scaled PD−L1 expression
scaled CTLA4 expression
scaled TIGIT expression
***
****

◂**Fig. 7** Drug sensitivity and immunotherapy cohort validation of PaFMS. (**A**) Boxplot showing 4 drugs with significantly higher IC50 values and 4 drugs with significantly lower IC50 values in the high-risk group. (**B**) Survival analysis of high- and low-risk samples in the IMvigor210 cohort. (**C**) Boxplot showing the difference of risk score in Anti-PD-L1 response and Anti-PD-L1 no response groups. (**D**) Proportion of anti-PD-L1 immunotherapy responses detected in high risk and low risk samples. (**E**) Boxplot showing the difference of PD1, PD-L1, CTLA4 and TIGIT expression in high-risk and low-risk groups

$R = 0.63$, $p < 0.001$) and the myoCAF-c1 spatial regions (Fig. 8C-D, S4B-E). At the protein level, expression of the four genes was assessed using data from the HPA database, although protein information for *IGFBP3* was unavailable (Fig. 8E). Notably, *TMEM158* showed high expression in primary PDAC tissues, reduced levels in liver metastases, and was absent in adjacent normal pancreas (Fig. 8E). Collectively, these results validate PaFMS signature genes across single-cell, spatial transcriptomic, and proteomic modalities, offering potential molecular targets for immunotherapy and precision medicine in PDAC.

Discussion

CAFs in PDAC play pivotal roles in tumor progression and become novel targets for anti-tumour interventions [9, 10]. However, the comprehensive landscape of CAF-specific membrane proteins remains largely undefined. In this study, by integrating scRNA-seq, spatial transcriptomics, bulk transcriptomic profiling, and protein-level validation, we identified a panel of PDAC CAF–specific membranes and established a prognostic model, termed PaFMS. This model was strongly associated with tumor proliferation, immune suppression, and therapeutic responses to both chemotherapy and immunotherapy.

Recent studies have highlighted the therapeutic potential of targeting CAF-derived genes in PDAC [48]. CAFs secrete collagen and other ECM components that contribute to treatment resistance [48]. Wu et al. reported that CAFs remodel the ECM and promote EMT in PDAC via the POSTN–ITGAV/ITGB5 axis [49]. Consistent with this, our study found that myoCAF-c1 expresses ECM-related membrane genes such as *LUM* [50], and is enriched in EMT pathways. Furthermore, recent work suggests that targeting CAF membrane proteins in the TME can enhance CAR-T cell efficacy in PDAC [19]. However, current knowledge of CAF-specific membrane proteins remains incomplete. Here, by comparing adjacent normal pancreas and liver metastases, we identified a PDAC-enriched CAF subtype—myoCAF-c1—characterized by high expression of membrane genes such as *COL11A1*, and *MMP11*, which is associated with EMT and tumor progression [51, 52].

Furthermore, we developed the PaFMS signature from 11 prognostically relevant membrane genes in the myoCAF-c1 cluster, with *PLAU*, *TMEM158*, and *TRIM59* as its representative features. A recent study found that stromal PLAU can drive tumor progression, providing a novel therapeutic target for triple-negative breast cancer [53]. Liu et al. further reported that *PLAU* participates in cancer-associated immunosuppression [54]. *TMEM158* has been reported to be involved in the progression of various cancers, including intrahepatic cholangiocarcinoma [55], ovarian cancer [56], and glioblastoma [57]. Consistent with these findings, our study identified those genes as PaFMS signatures, with PaFMS associated with tumor progression and reduced T/B cell infiltration in the PDAC TME.

Notably, PaFMS can be interpreted as a stromal remodeling–immune regulatory axis rather than isolated gene–outcome correlations. Specifically, the positive-coefficient components, such as TRIM59, PLAU, and PERP, are consistent with pro-tumor signaling and proteolysis-associated matrix remodeling programs reported in PDAC [58–60]. These molecular programs are known to influence ECM remodeling, EMT, and immune cell exclusion within the TME. Based on this synthesis, we propose a testable working hypothesis that myoCAF-c1 states promote a uPA/PLAU-centered remodeling program that facilitates EMT and contributes to an immunosuppressive microenvironment in PDAC [58, 59].

Considering that PaFMS is a prognostic model, we validated its predictive robustness across five independent cohorts. Recent studies have proposed other prognostic models for PDAC or pancreatic cancer, such as the T cell marker genes score (TMGS), which achieved mean AUCs of 0.658, 0.718, and 0.768 for 1-, 2-, and 3-year OS, respectively, in four independent validation cohorts [61]. Similarly, Ding et al. developed a membrane-associated gene prognostic signature (MaGPS), which yielded mean AUCs of 0.600, 0.627, and 0.617 for 1-, 2-, and 3-year OS, respectively, in three validation cohorts [46]. Compared with TMGS [61] and MaGPS [46], our PaFMS signature demonstrated greater robustness and higher predictive accuracy for 1-, 2-, and 3-year OS (short-term), with mean AUCs of 0.759, 0.789, and 0.799, respectively, across five independent validation cohorts. Notably, PaFMS also demonstrated strong predictive ability for 5-year OS, with a mean AUC of 0.820. We further compared PaFMS with two additional models: the tumor-associated macrophage signature (TAMS) [62] and the fibroblast-related prognostic signature (FRPS) [63]. The tumor-associated macrophage signature (TAMS) developed by Fan et al. achieved a mean 5-year AUC of 0.565 [62], while the fibroblast-related prognostic signature (FRPS) developed by Wang et al. achieved 0.805 [63]. In comparison, PaFMS outperformed both TAMS and FRPS in 5-year (long-term)

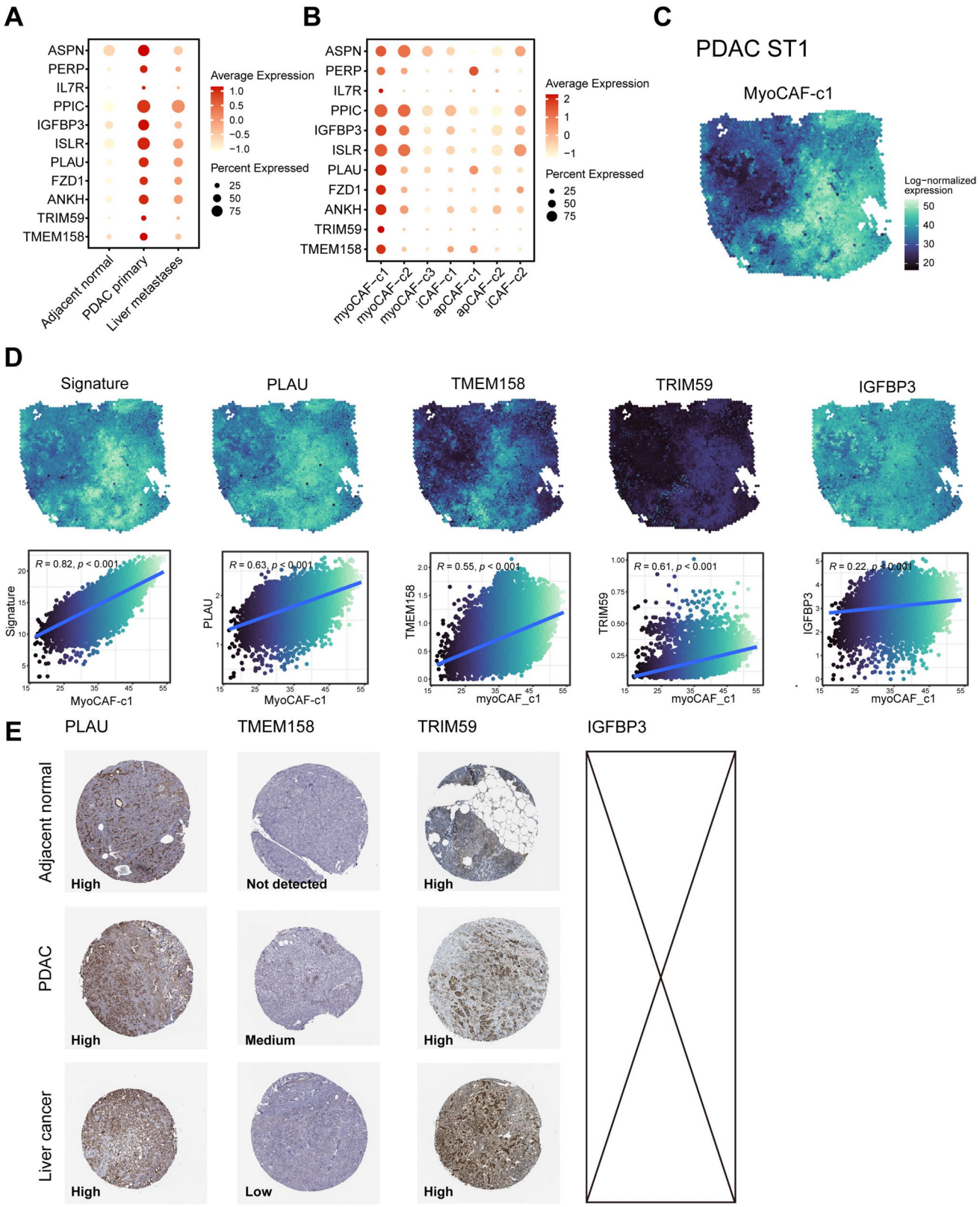

survival prediction. Collectively, these findings highlight PaFMS as a compelling and robust independent prognostic factor for PDAC.

Prior studies have shown that senescent CAFs can suppress $CD8^+$ T cell activation and diminish immunotherapy responsiveness [64], and that CAFs can promote early PDAC

◂**Fig. 8** Single-cell, spatial and protein profiling analysis of PaFMS target genes. (**A**) Bubble plot showing the expression of PaFMS target genes across all tissues. (**B**) Bubble plot showing the expression of PaFMS target genes across all fibroblast sub-clusters. (**C**) Spatial distribution of myoCAF-c1 feature score in PDAC ST1 sample. (**D**) Spatial distribution of PaFMS signature score and PaFMS target genes and the correlation between PaFMS signature score, PaFMS target genes and myoCAF-c1 feature score in PDAC ST1 sample. (**E**) Protein expression of the 3 PaFMS signature genes in PDAC, normal pancreas and liver cancer tissues based on the human protein atlas (HPA). The IHC staining levels was categorized as "Not detected", "Low", "Medium", or "High"

invasion through the SOX4/MMP11 axis [65]. These findings align with the functional characteristics of our PaFMS, which is strongly associated with EMT and reduced T/B-cell infiltration. Moreover, PaFMS also has potential therapeutic implications. In the high-risk group, chemotherapeutic agents such as selumetinib (AZD6244) exhibited lower predicted IC50 values; notably, selumetinib has been applied in the treatment of various cancers [66–68], suggesting that patients in this group may derive therapeutic benefit from selumetinib. Conversely, patients in the low-risk group appeared to benefit more from anti–PD-L1 immunotherapy. Thus, these findings support our assessment of drug sensitivity and highlight the potential of PaFMS as a predictive biomarker for guiding personalized therapy in PDAC.

However, several limitations should be acknowledged. First, although protein-level evidence from the HPA was incorporated, functional validation of the identified membrane genes was not performed, and further experimental studies will be required to confirm their biological roles and mechanistic relevance. Second, while PaFMS demonstrated consistent prognostic performance across multiple independent retrospective cohorts, prospective validation in multicenter PDAC cohorts will be necessary to establish its clinical applicability. Third, the IMvigor210 cohort comprises urothelial carcinoma rather than PDAC; therefore, immunotherapy-related observations from this cohort should be considered supportive and hypothesis-generating, requiring validation in PDAC-specific immunotherapy datasets. Finally, although PaFMS was compared with several published transcriptomic signatures, comprehensive benchmarking against routinely used clinical prognostic factors such as anatomical staging, histologic grade, and serum CA19-9 levels remains warranted.

In conclusion, by integrating single-cell and spatial transcriptomics, we identified a PDAC-enriched CAF subset, myoCAF-c1. Based on these CAF-specific membrane genes, we developed PaFMS, a robust prognostic signature that accurately predicts survival across multiple cohorts. PaFMS stratification also correlates with distinct drug sensitivities and immune checkpoint expression, underscoring its potential to guide both targeted and immunotherapeutic strategies. Collectively, our findings position PaFMS as a clinically relevant biomarker and a promising source of therapeutic targets for precision oncology in PDAC.

Supplementary Information The online version contains supplementary material available at https://doi.org/10.1007/s00109-026-02669-7.

Acknowledgements The authors are thankful to Ms. Ying Chen for her valuable suggestions.

Authors contributions Leshi Zhuang: Conceptualization, Formal analysis, Visualization, Writing—original draft. Wei Zhang: Formal analysis, Visualization, Validation, Writing—original draft. Jun Wu: Conceptualization, Methodology, Writing – review & editing. Jian Cao: Methodology, Data curation. Liang Feng: Data curation, Investigation. Shubo Cao: Conceptualization, Supervision, Resources, Writing – review & editing.

Funding The authors did not receive support from any organization for the submitted work.

Data availability scRNA-seq data can be accessed from GEO under accession numbers GSE154778, GSE197177, and GSE212966, and spatial transcriptomics data from GSE202740. Bulk RNA-seq and clinical information can be obtained from the TCGA-PAAD cohort, ICGC-PACA-AU, and GEO under accession number GSE21501, GSE57495, GSE62452, GSE71729, and GSE78220. For any other reasonable requests, please contact the corresponding author.

Code availability Details of the software and parameters used in this study are provided in the Methods section. The relevant code will be made publicly available on GitHub upon acceptance of the manuscript (https://github.com/shikizv/PaFMS).

Declarations

Ethics Not applicable.

Competing interests The authors declare no competing interests.

References

1. Halbrook CJ, Lyssiotis CA, Pasca di Magliano M, Maitra A (2023) Pancreatic cancer: advances and challenges. Cell 186(8):1729–1754
2. Aquino AF, Runa F, Shoma JF, Todd A, Wallace M, de Barros NR, Kelber JA (2024) Multidimensional screening of pancreatic

cancer spheroids reveals vulnerabilities in mitotic and cell-matrix adhesion signaling that associate with metastatic progression and decreased patient survival. Biochem Biophys Res Commun 703:149575
3. Hartupee C, Nagalo BM, Chabu CY, Tesfay MZ, Coleman-Barnett J, West JT, Moaven O (2024) Pancreatic cancer tumor microenvironment is a major therapeutic barrier and target. Front Immunol 15:1287459
4. Kleeff J, Korc M, Apte M, La Vecchia C, Johnson CD, Biankin AV, Neale RE, Tempero M, Tuveson DA, Hruban RH et al (2016) Pancreatic cancer. Nat Rev Dis Primers 2:16022
5. Gong R, Chen Y, Li C, Zhang H, Liu Z, Yu Q (2025) Targeting myeloid cells in pancreatic ductal adenocarcinoma: from primary tumors to liver metastasis. Front Immunol 16:1555036
6. Zambirinis CP, Midya A, Chakraborty J, Chou JF, Zheng J, McIntyre CA, Koszalka MA, Wang T, Do RK, Balachandran VP et al (2022) Recurrence after resection of pancreatic cancer: can radiomics predict patients at greatest risk of liver metastasis? Ann Surg Oncol 29(8):4962–4974
7. Dzobo K, Senthebane DA, Dandara C (2023) The tumor microenvironment in tumorigenesis and therapy resistance revisited. Cancers (Basel) 15(2):376
8. Borzone FR, Giorello MB, Sanmartin MC, Yannarelli G, Martinez LM, Chasseing NA (2024) Mesenchymal stem cells and cancer-associated fibroblasts as a therapeutic strategy for breast cancer. Br J Pharmacol 181(2):238–256
9. Luo H, Xia X, Huang LB, An H, Cao M, Kim GD, Chen HN, Zhang WH, Shu Y, Kong X et al (2022) Pan-cancer single-cell analysis reveals the heterogeneity and plasticity of cancer-associated fibroblasts in the tumor microenvironment. Nat Commun 13(1):6619
10. Zhang T, Ren Y, Yang P, Wang J, Zhou H (2022) Cancer-associated fibroblasts in pancreatic ductal adenocarcinoma. Cell Death Dis 13(10):897
11. Wu Z, Uhl B, Gires O, Reichel CA (2023) A transcriptomic pan-cancer signature for survival prognostication and prediction of immunotherapy response based on endothelial senescence. J Biomed Sci 30(1):21
12. Costa A, Kieffer Y, Scholer-Dahirel A, Pelon F, Bourachot B, Cardon M, Sirven P, Magagna I, Fuhrmann L, Bernard C et al (2018) Fibroblast heterogeneity and immunosuppressive environment in human breast cancer. Cancer Cell 33(3):463-479.e410
13. Bruciamacchie M, Garambois V, Vie N, Bessede T, Michaud HA, Chepeaux LA, Gros L, Bonnefoy N, Robin M, Brager D et al (2025) ATR inhibition potentiates FOLFIRINOX cytotoxic effect in models of pancreatic ductal adenocarcinoma by remodelling the tumour microenvironment. Br J Cancer 132(2):222–235
14. Wu J, Liu Y, Fu Q, Cao Z, Ma X, Li X (2024) Characterization of tumor-associated endothelial cells and the development of a prognostic model in pancreatic ductal adenocarcinoma. Biochim Biophys Acta Gen Subj 1868(3):130545
15. Zhu X, You S, Du X, Song K, Lv T, Zhao H, Yao Q (2023) LRRC superfamily expression in stromal cells predicts the clinical prognosis and platinum resistance of ovarian cancer. BMC Med Genomics 16(1):10
16. Pellinen T, Paavolainen L, Martín-Bernabé A, Papatella Araujo R, Strell C, Mezheyeuski A, Backman M, La Fleur L, Brück O, Sjölund J et al (2023) Fibroblast subsets in non-small cell lung cancer: associations with survival, mutations, and immune features. J Natl Cancer Inst 115(1):71–82
17. Peng K, Zhang Y, Liu D, Chen J (2023) MMP2 is a immunotherapy related biomarker and correlated with cancer-associated fibroblasts infiltrate in melanoma. Cancer Cell Int 23(1):26
18. Wu H, Xiang Z, Huang G, He Q, Song J, Dou R, Yang C, Wang S, Xiong B (2023) BGN/FAP/STAT3 positive feedback loop mediated mutual interaction between tumor cells and mesothelial cells contributes to peritoneal metastasis of gastric cancer. Int J Biol Sci 19(2):465–483
19. Wehrli M, Guinn S, Birocchi F, Kuo A, Sun Y, Larson RC, Almazan AJ, Scarfò I, Bouffard AA, Bailey SR et al (2024) Mesothelin CAR T cells secreting anti-FAP/anti-CD3 molecules efficiently target pancreatic adenocarcinoma and its stroma. Clin Cancer Res 30(9):1859–1877
20. Nakatsura T, Takenouchi K, Kataoka J, Ito Y, Kikuchi S, Kinoshita H, Ohnuki K, Suzuki T, Tsukamoto N (2025) Expression profiles of five common cancer membrane protein antigens collected for the development of cocktail CAR-T cell therapies applicable to most solid cancer patients. Int J Mol Sci 26(5):2145
21. Mitchell MJ, Billingsley MM, Haley RM, Wechsler ME, Peppas NA, Langer R (2021) Engineering precision nanoparticles for drug delivery. Nat Rev Drug Discov 20(2):101–124
22. Kuhlmann L, Cummins E, Samudio I, Kislinger T (2018) Cell-surface proteomics for the identification of novel therapeutic targets in cancer. Expert Rev Proteomics 15(3):259–275
23. Khongorzul P, Ling CJ, Khan FU, Ihsan AU, Zhang J (2020) Antibody-Drug conjugates: a comprehensive review. Mol Cancer Res 18(1):3–19
24. Maia A, Tarannum M, Lérias JR, Piccinelli S, Borrego LM, Maeurer M, Romee R, Castillo-Martin M (2024) Building a better defense: expanding and improving natural killer cells for adoptive cell therapy. Cells 13(5):451
25. Tu B, Wu J, Zhang W, Tang H, Dai T, Xie B (2025) A novel cancer-associated membrane signature predicts prognosis and therapeutic response for lung adenocarcinoma. Sci Rep 15(1):25482
26. Meng S, Hara T, Miura Y, Ishii H (2024) Fibroblast activation protein constitutes a novel target of chimeric antigen receptor T-cell therapy in solid tumors. Cancer Sci 115(11):3532–3542
27. Niu W, Wang B, Zhang Y, Wang C, Cao J, Li J, He Y, Lei P (2024) Efficacy and safety evaluation of cross-reactive Fibroblast activation protein scFv-based CAR-T cells. Front Immunol 15:1433679
28. Xu Q, Chen S, Hu Y, Huang W (2021) Single-cell RNA transcriptome reveals the intra-tumoral heterogeneity and regulators underlying tumor progression in metastatic pancreatic ductal adenocarcinoma. Cell Death Discov 7(1):331
29. Peng J, Sun BF, Chen CY, Zhou JY, Chen YS, Chen H, Liu L, Huang D, Jiang J, Cui GS et al (2019) Single-cell RNA-seq highlights intra-tumoral heterogeneity and malignant progression in pancreatic ductal adenocarcinoma. Cell Res 29(9):725–738
30. Zhang S, Fang W, Zhou S, Zhu D, Chen R, Gao X, Li Z, Fu Y, Zhang Y, Yang F et al (2023) Single cell transcriptomic analyses implicate an immunosuppressive tumor microenvironment in pancreatic cancer liver metastasis. Nat Commun 14(1):5123
31. Wu J, Dai T, Li Z, Pan M, Zhang W, Chen H, Zheng G, Qiao L, Lian Q, Liu Y et al (2025) Integrating multi-modal transcriptomics identifies cellular subtypes with distinct roles in PDAC progression. Cell Oncol (Dordr) 48(5):1571–92
32. Chen MM, Gao Q, Ning H, Chen K, Gao Y, Yu M, Liu CQ, Zhou W, Pan J, Wei L et al (2025) Integrated single-cell and spatial transcriptomics uncover distinct cellular subtypes involved in neural invasion in pancreatic cancer. Cancer Cell 43(9):1656-1676.e1610
33. Xue M, Zhu Y, Jiang Y, Han L, Shi M, Su R, Wang L, Xiong C, Wang C, Wang T et al (2023) Schwann cells regulate tumor cells and cancer-associated fibroblasts in the pancreatic ductal adenocarcinoma microenvironment. Nat Commun 14(1):4600

34. Chen K, Wang Q, Liu X, Tian X, Dong A, Yang Y (2023) Immune profiling and prognostic model of pancreatic cancer using quantitative pathology and single-cell RNA sequencing. J Transl Med 21(1):210
35. Lin W, Noel P, Borazanci EH, Lee J, Amini A, Han IW, Heo JS, Jameson GS, Fraser C, Steinbach M et al (2020) Single-cell transcriptome analysis of tumor and stromal compartments of pancreatic ductal adenocarcinoma primary tumors and metastatic lesions. Genome Med 12(1):80
36. Balar AV, Galsky MD, Rosenberg JE, Powles T, Petrylak DP, Bellmunt J, Loriot Y, Necchi A, Hoffman-Censits J, Perez-Gracia JL et al (2017) Atezolizumab as first-line treatment in cisplatin-ineligible patients with locally advanced and metastatic urothelial carcinoma: a single-arm, multicentre, phase 2 trial. Lancet 389(10064):67–76
37. Hao Y, Stuart T, Kowalski MH, Choudhary S, Hoffman P, Hartman A, Srivastava A, Molla G, Madad S, Fernandez-Granda C et al (2024) Dictionary learning for integrative, multimodal and scalable single-cell analysis. Nat Biotechnol 42(2):293–304
38. Korsunsky I, Millard N, Fan J, Slowikowski K, Zhang F, Wei K, Baglaenko Y, Brenner M, Loh PR, Raychaudhuri S (2019) Fast, sensitive and accurate integration of single-cell data with Harmony. Nat Methods 16(12):1289–1296
39. Zhao E, Stone MR, Ren X, Guenthoer J, Smythe KS, Pulliam T, Williams SR, Uytingco CR, Taylor SEB, Nghiem P et al (2021) Spatial transcriptomics at subspot resolution with BayesSpace. Nat Biotechnol 39(11):1375–1384
40. Hu C, Li T, Xu Y, Zhang X, Li F, Bai J, Chen J, Jiang W, Yang K, Ou Q et al (2023) CellMarker 2.0: an updated database of manually curated cell markers in human/mouse and web tools based on scRNA-seq data. Nucleic Acids Res 51(D1):D870-d876
41. Elyada E, Bolisetty M, Laise P, Flynn WF, Courtois ET, Burkhart RA, Teinor JA, Belleau P, Biffi G, Lucito MS et al (2019) Cross-species single-cell analysis of pancreatic ductal adenocarcinoma reveals antigen-presenting cancer-associated fibroblasts. Cancer Discov 9(8):1102–1123
42. Qiu X, Mao Q, Tang Y, Wang L, Chawla R, Pliner HA, Trapnell C (2017) Reversed graph embedding resolves complex single-cell trajectories. Nat Methods 14(10):979–982
43. Jin S, Guerrero-Juarez CF, Zhang L, Chang I, Ramos R, Kuan C-H, Myung P, Plikus MV, Nie Q (2021) Inference and analysis of cell-cell communication using CellChat. Nat Commun 12(1):1088
44. Newman AM, Liu CL, Green MR, Gentles AJ, Feng W, Xu Y, Hoang CD, Diehn M, Alizadeh AA (2015) Robust enumeration of cell subsets from tissue expression profiles. Nat Methods 12(5):453–457
45. Geeleher P, Cox N, Huang RS (2014) pRRophetic: an R package for prediction of clinical chemotherapeutic response from tumor gene expression levels. PLoS ONE 9(9):e107468
46. Ding Z, Wu J, Ye Y, Zhong Y, Yan L, Wang P (2025) A novel signature predicts prognosis in pancreatic cancer based on tumor membrane-associated genes. Heliyon 11(4):e42791
47. Zhang D, Duque-Jimenez J, Facchinetti F, Brixi G, Rhee K, Feng WW, Jänne PA, Zhou X (2025) Transferrin receptor targeting chimeras for membrane protein degradation. Nature 638(8051):787–795
48. Masuda H (2025) Cancer-associated fibroblasts in cancer drug resistance and cancer progression: a review. Cell Death Discov 11(1):341
49. Wu Y, Li S, Yu H, Zhang S, Yan L, Guan X, Xu W, Wang Z, Lv A, Tian X et al (2025) Integrative single-cell and spatial transcriptomics analysis reveals ECM-remodeling cancer-associated fibroblast-derived POSTN as a key mediator in pancreatic ductal adenocarcinoma progression. Int J Biol Sci 21(8):3573–3596
50. Cui X, Huo D, Wang Q, Wang Y, Liu X, Zhao K, You Y, Zhang J, Kang C (2024) RUNX1/NPM1/H3K4me3 complex contributes to extracellular matrix remodeling via enhancing FOSL2 transcriptional activation in glioblastoma. Cell Death Dis 15(1):98
51. Ma G, Li G, Fan W, Xu Y, Song S, Guo K, Liu Z (2021) Circ-0005105 activates COL11A1 by targeting miR-20a-3p to promote pancreatic ductal adenocarcinoma progression. Cell Death Dis 12(7):656
52. Wang Z, Guo X, Li X, Wang J, Zhang N, Amin B, Xu G, Zhu B (2025) Cancer-associated fibroblast-derived MMP11 promotes tumor progression in pancreatic cancer. Cancer Sci 116(3):643–655
53. Zou J, Zhang J, Li Y, Yuan B, Wang Y, Qi Y, Wang Q, Qin W, Yuan X, Xu B (2025) Stromal PLAU mediates tumor progression and informs a novel therapeutic target in triple-negative breast cancer. Cancer Cell Int 25(1):259
54. Liu L, Huang H, Cheng B, Xie H, Peng W, Cui H, Liang J, Cao M, Yang Y, Chen W et al (2025) Revealing the role of cancer-associated fibroblast senescence in prognosis and immune landscape in pancreatic cancer. iScience 28(1):111612
55. Chen P, Yang J, Jin S, Li Y, Li D, Zhong C, Zhang Y, Xia Q, Fan X, Lin H (2025) TMEM158 promotes ICC metastasis via inducing lactic acid mediated reduction of actin skeleton stiffness of ICC cells. J Adv Res
56. Zhu X, Liu T, Yin X (2024) TMEM158, as plasma cfRNA marker, promotes proliferation and doxorubicin resistance in ovarian cancer. Pharmacogenomics J 24(6):34
57. Li J, Wang X, Chen L, Zhang J, Zhang Y, Ren X, Sun J, Fan X, Fan J, Li T et al (2024) Correction: TMEM158 promotes the proliferation and migration of glioma cells via STAT3 signaling in glioblastomas. Cancer Gene Ther 31(3):495–496
58. Li R, Weng L, Liu B, Zhu L, Zhang X, Tian G, Hu L, Li Q, Jiang S, Shang M (2020) TRIM59 predicts poor prognosis and promotes pancreatic cancer progression via the PI3K/AKT/mTOR-glycolysis signaling axis. J Cell Biochem 121(2):1986–1997
59. Hosen SMZ, Uddin MN, Xu Z, Buckley BJ, Perera C, Pang TCY, Mekapogu AR, Moni MA, Notta F, Gallinger S et al (2022) Metastatic phenotype and immunosuppressive tumour microenvironment in pancreatic ductal adenocarcinoma: key role of the urokinase plasminogen activator (PLAU). Front Immunol 13:1060957
60. Dasgupta A, Arneson-Wissink PC, Schmitt RE, Cho DS, Ducharme AM, Hogenson TL, Krueger EW, Bamlet WR, Zhang L, Razidlo GL et al (2022) Anticachectic regulator analysis reveals Perp-dependent antitumorigenic properties of 3-methyladenine in pancreatic cancer. JCI Insight 7(2):e153842
61. Zheng H, Li Y, Zhao Y, Jiang A (2023) Single-cell and bulk RNA sequencing identifies T cell marker genes score to predict the prognosis of pancreatic ductal adenocarcinoma. Sci Rep 13(1):3684
62. Fan Y, Wu L, Qiu X, Shi H, Wu L, Lin J, Lin J, Teng T (2025) Single-cell RNA-seq analysis reveals microenvironmental infiltration of myeloid cells and pancreatic prognostic markers in PDAC. Discover Oncol 16(1):81
63. Wang W, Li H, Gong J, Liu Y (2025) Identification of a fibroblast-derived gene signature reveals prognostic and therapeutic insights in pancreatic cancer. Clin Exp Med 25(1):253
64. Belle JI, Sen D, Baer JM, Liu X, Lander VE, Ye J, Sells BE, Knolhoff BL, Faiz A, Kang LI et al (2024) Senescence defines a distinct subset of myofibroblasts that orchestrates immunosuppression in pancreatic cancer. Cancer Discov 14(7):1324–1355

65. Ge F, Zeng C, Wang J, Liu X, Zheng C, Zhang H, Yang L, Yang B, Zhu H, He Q (2024) Cancer-associated fibroblasts drive early pancreatic cancer cell invasion via the SOX4/MMP11 signalling axis. Biochim Biophys Acta Mol Basis Dis 1870(1):166852
66. Oxnard GR, Yang JC, Yu H, Kim SW, Saka H, Horn L, Goto K, Ohe Y, Mann H, Thress KS et al (2020) TATTON: a multi-arm, phase Ib trial of osimertinib combined with selumetinib, savolitinib, or durvalumab in EGFR-mutant lung cancer. Ann Oncol 31(4):507–516
67. Fangusaro J, Onar-Thomas A, Young Poussaint T, Wu S, Ligon AH, Lindeman N, Banerjee A, Packer RJ, Kilburn LB, Goldman S et al (2019) Selumetinib in paediatric patients with BRAF-aberrant or neurofibromatosis type 1-associated recurrent, refractory, or progressive low-grade glioma: a multicentre, phase 2 trial. Lancet Oncol 20(7):1011–1022
68. Wächter S, Wunderlich A, Greene BH, Roth S, Elxnat M, Fellinger SA, Verburg FA,

Authors and Affiliations

Leshi Zhuang[1] · Wei Zhang[2] · Jun Wu[2,3] · Jian Cao[4] · Liang Feng[4] · Shubo Cao[1]

✉ Shubo Cao
13807374946@163.com

[1] Department of Hepatobiliary, Pancreatic and Splenic Surgery, Yiyang Central Hospital, No. 118, Kangfu North Road, Heshan District, Yiyang 413000, Hunan Province, China

[2] Institute for Brain Research and Rehabilitation, South China Normal University, Guangzhou 510631, Guangdong Province, China

[3] School of Biomedical Science, Hunan University, Hunan Province, Changsha 410082, China

[4] General Surgery Department, Yiyang Central Hospital, Hunan Province, Yiyang 413000, China